The impact of calibration phantom errors on dual-energy digital mammography

2008 Phys. Med. Biol. 53 6321

(http://iopscience.iop.org/0031-9155/53/22/004)

IOP PUBLISHING PHYSICS IN MEDICINE AND BIOLOGY

Phys. Med. Biol. **53** (2008) 6321–6336 doi:10.1088/0031-9155/53/22/004

The impact of calibration phantom errors on dual-energy digital mammography

Xuanqin Mou[1], Xi Chen[1], Lijun Sun[2], Hengyong Yu[3], Zhen Ji[4] and Lei Zhang[5]

[1] Institute of Image Processing & Pattern Recognition, Xi'an Jiaotong University, Xi'an, Shaanxi 710049, People's Republic of China
[2] Department of Radiology, Xijing Hospital, Fourth Military Medical University, Xi'an, Shaanxi 710032, People's Republic of China
[3] Biomedical Imaging Division, VT-WFU School of Biomedical Engineering and Science, Virginia Tech., Blacksburg, VA 240601, USA
[4] Department of Information Engineering, Shenzhen University, Shenzhen 518060, People's Republic of China
[5] Department of Computing, Hong Kong Polytechnic University, Hung Hom, Kowloon, Hong Kong

E-mail: xqmou@mail.xjtu.edu.cn

Received 23 March 2008, in final form 3 August 2008
Published 20 October 2008
Online at stacks.iop.org/PMB/53/6321

Abstract

Microcalcification is one of the earliest and main indicators of breast cancer. Because dual-energy digital mammography could suppress the contrast between the adipose and glandular tissues of the breast, it is considered a promising technique that will improve the detection of microcalcification. In dual-energy digital mammography, the imaged object is a human breast, while in calibration measurements only the phantoms of breast tissue equivalent materials are available. Consequently, the differences between phantoms and breast tissues will lead to calibration phantom errors. Based on the dual-energy imaging model, formulae of calibration phantom errors are derived in this paper. Then, this type of error is quantitatively analyzed using publicly available data and compared with other types of error. The results demonstrate that the calibration phantom error is large and dominant in dual-energy mammography, seriously decreasing calculation precision. Further investigations on the physical meaning of calibration phantom error reveal that the imaged objects with the same glandular ratio have identical calibration phantom error. Finally, an error correction method is proposed based on our findings.

(Some figures in this article are in colour only in the electronic version)

1. Introduction

Breast cancer is a deadly disease that adversely affects the lives of many people, primarily women. Microcalcification is one of the earliest and main indicators of breast cancer, and mammography is the gold standard for breast cancer screening. Thus, the visualization and detection of microcalcifications in mammography play a crucial role in reducing the rate of mortality from breast cancer. Microcalcifications are usually smaller than 1.0 mm and mainly composed of calcium compounds (Fandos-Morera *et al* 1988) such as apatite, calcium oxalate and calcium carbonate. Microcalcifications have greater x-ray attenuation coefficients than the surrounding breast tissues, so they are more visible on homogeneous soft-tissue backgrounds. However, the visualization of microcalcifications could be obscured in mammograms because of overlapping of tissue structures. Tissue structures in mammograms arise from the differences of the x-ray attenuation coefficients between adipose tissue, glandular tissue, ducts, vessels and soft-tissue masses. Microcalcifications, especially smaller ones, are extremely difficult to discriminate even if the signal-to-noise ratio is high (Brettle and Cowen 1994). Therefore, microcalcification detection in mammography suffers from a high false-negative rate (Soo *et al* 2005).

Dual-energy digital mammography is considered as a prospective technique to improve the detection of microcalcification. The healthy breast is mainly composed of adipose, epithelial and stroma tissues which can be grouped into two attenuating types: adipose tissue and glandular tissue. In dual-energy digital mammography, high- and low-energy images of the breast are acquired using two different x-ray spectra. By exploiting the difference in x-ray attenuation between different materials at different x-ray energies, the high- and low-energy images can be synthesized to suppress the contrast between adipose and glandular tissues and subsequently generate the dual-energy calcification image. Under ideal imaging conditions, when the imaging data are free of scatter and other biases, dual-energy digital mammography could be used to determine the thickness of microcalcification and the breast glandular ratio (Lemacks *et al* 2002). This quantitative information can be incorporated into computer-aided detection algorithms to enhance mammographic interpretation.

However, a lot of research must be carried out prior to applying dual-energy digital mammography in clinics. Early research on the feasibility of dual-energy mammography includes optimal high- and low-energy spectra selection (Johns and Yaffe 1985), selection of inverse-map functions (Cardinal and Fenster 1990), influence of detectors (Chakraborty and Barnes 1989, Boone *et al* 1990, Brettle and Cowen 1994) and experimental studies (Johns *et al* 1985, Brettle and Cowen 1994). Lemacks *et al* (2002) presented a theoretical framework to calculate the (quantum) noise in dual-energy calcification image and made numerical analysis as well. Their results were presented in terms of contrast-to-noise ratio under various imaging conditions, including the x-ray spectra, microcalcification size, tissue composition and breast thickness. Based on the work of Lemacks *et al* (2002), Kappadath *et al* made a series of investigations on dual-energy digital mammography (Kappadath and Shaw 2003, 2004, 2005, Kappadath *et al* 2004, 2005). Kappadath and Shaw (2003) investigated various inverse-map functions for dual-energy digital mammography, and concluded that the mean fitting error is $\sim$50 μm and the max fitting error is $\sim$150 μm for the microcalcification thickness when using the cubic or conic functions. Kappadath and Shaw (2005) developed a scatter and nonuniformity correction technique for dual-energy digital mammography. In their implementation on the clinical equipment, microcalcifications in 300–355 μm range were clearly visible in dual-energy calcification images. The microcalcification size threshold decreased to 250–280 μm when the visible criteria were lowered to barely eyesight. Dual-

energy digital mammography has also been investigated and evaluated by other investigators (Bliznakova *et al* 2006, Brandan and Ramirez-R 2006, Taibi *et al* 2003).

In dual-energy digital mammography, there are two necessary steps: the first step is calibration, which estimates the polynomial coefficients using calibration data, while the second step is the calculation of the component information of the imaged object. When dual-energy digital mammography is used clinically, the imaged object is a human breast. In calibration, however, only phantoms of a breast tissue equivalent material can be used. The composition and density differences between the phantoms and breast tissues cause differences in linear attenuation coefficients, which consequently lead to so-called calibration phantom errors. The error was first indicated and investigated by Mou and Chen (2007) and consisted of two parts: microcalcification thickness error and glandular ratio error. The small differences in linear attenuation coefficients between calibration phantoms and breast tissues lead to huge calibration phantom errors in the final results. The phantom materials, like PMMA, polyethylene and RMI phantoms, are not suitable for calibration of dual-energy digital mammography in clinics. Comparably, CIRS phantoms are a better choice.

In reality, the elemental composition ratio of human breast varies greatly (Hammerstein *et al* 1979). The differences in linear attenuation coefficients between calibration phantoms and breast tissues are inevitable. Therefore, calibration phantom errors cannot be removed solely by redesigning calibration phantoms. This study systematically analyzes the calibration phantom errors, investigates their physical meaning and develops possible error correction methods.

2. Theory

This section first presents the imaging principles and the physical model of dual-energy digital mammography and then develops the formulae for calibration phantom errors.

2.1. Imaging principle

The principles of dual-energy imaging have been discussed extensively in the literature (Alvarez and Macovski 1976, Lehmann *et al* 1981, Brody *et al* 1981, Johns and Yaffe 1985, Gingold and Hasegawa 1992). In the medical diagnostic x-ray imaging modality, x-ray attenuation includes photoemission and Compton scattering. The linear attenuation coefficient $\mu(E)$ is (Alvarez and Macovski 1976)

$$\mu(E) = b_{pu} E^{-3} + b_{du} f_{\mathrm{KN}}(E), \tag{1}$$

where $f_{\mathrm{KN}}(E)$ is the Klein–Nishina function,

$$f_{\mathrm{KN}}(E) = \frac{1+\alpha}{\alpha}\left[\frac{2(1+\alpha)}{1+2\alpha} - \frac{1}{\alpha}\ln(1+2\alpha)\right] + \frac{1}{2\alpha}\ln(1+2\alpha) - \frac{(1+3\alpha)}{(1+2\alpha)^2}, \tag{2}$$

and $\alpha = E/510.975$. The attenuation coefficient of any material above the k-edge can be approximated by equation (1). Because the atomic numbers of the elements in human body are small and their k-edge energies are low, equation (1) is valid for medical diagnostic x-ray imaging. The term E^{-3} approximates the energy dependence of the photoelectric interaction, and $f_{\mathrm{KN}}(E)$ gives the energy dependence of the total cross-section for Compton scattering. The dependences of b_{pu} and b_{du} on physical parameters are given below:

$$b_{pu} \approx K_1 \frac{\rho}{A} Z^n, \qquad b_{du} \approx K_2 \frac{\rho}{A} Z, \tag{3}$$

where K_1 and K_2 are constants, ρ is the mass density, $n \approx 4$, A is the atomic weight and Z is the atomic number. If the imaged object is composed of two known materials, A with thickness

L_A and B with thickness L_B, the full object thickness is $L = L_A + L_B$ and the attenuation $M(E)$ of the imaged object can be expressed as (Lehmann *et al* 1981)

$$M(E) = b_p E^{-3} + b_d f_{\mathrm{KN}}(E), \tag{4}$$

where

$$b_p = b_{puA} L_A + b_{puB} L_B, \qquad b_d = b_{duA} L_A + b_{duB} L_B \tag{5}$$

and b_{puA}, b_{duA}, b_{puB} and b_{duB} are known quantities of the materials A and B.

An object can be imaged under high- and low-energy spectra:

$$f_j = -\ln\left(\int P_{0j}(E) \exp\left[-b_p E^{-3} - b_d f_{\mathrm{KN}}(E)\right] Q(E)\, \mathrm{d}E\right), \qquad j = h, l, \tag{6}$$

where $P_{0h}(E)$ and $P_{0l}(E)$ represent the incident x-ray photon fluence of high- and low-energy spectra, $Q(E)$ is the detector response, and f_h and f_l are the negative logarithm transmitted intensities of high- and low-energy spectra. b_p and b_d are defined in equation (5). If $P_{0h}(E)$, $P_{0l}(E)$ and $Q(E)$ are known, b_p and b_d of the object can be solved from equation (6), then L_A and L_B can be obtained based on equation (5). Since $P_{0h}(E)$ and $P_{0l}(E)$ are not easy to measure, in practice researchers often use inverse-map functions to solve L_A and L_B (Brody *et al* 1981):

$$\begin{cases} L_A = k_{A0} + k_{A1} f_h + k_{A2} f_l + k_{A3} f_h^2 + k_{A4} f_l^2 + k_{A5} f_h f_l + k_{A6} f_h^3 + k_{A7} f_l^3 \\ L_B = k_{B0} + k_{B1} f_h + k_{B2} f_l + k_{B3} f_h^2 + k_{B4} f_l^2 + k_{B5} f_h f_l + k_{B6} f_h^3 + k_{B7} f_l^3. \end{cases} \tag{7}$$

The coefficients k_{Ai} and k_{Bi}, $i = 0, \ldots, 7$, are determined using a calibration procedure (Lehmann *et al* 1981). By measuring the transmission intensities of various combinations of basic materials A and B with high- and low-energy spectra, the groups of calibration data (f_h, f_l, L_A, L_B) can be acquired to estimate the coefficients k_{Ai} and k_{Bi}. Accordingly, other forms of inverse-map functions, for example, implicit polynomials (Alvarez and Macovski 1976) and rational polynomials (Cardinal and Fenster 1990) can also be used for dual-energy calculations.

2.2. Physical model

Lemacks *et al* (2002) proposed a numerical framework to perform the dual-energy digital mammography calculation. They assumed that there are three attenuating materials in the breast: adipose tissue (thickness t_a), glandular tissue (thickness t_g) and microcalcification (thickness t_c). Depending on the distribution of materials, the transmitted fluence incident on the detector is given by

$$P(E) = P_0(E) \exp[-\mu_a(E) t_a - \mu_g(E) t_g - \mu_c(E) t_c], \tag{8}$$

where $P_0(E)$ and $P(E)$ are the incident photon fluence on the surface of the breast and the transmitted fluence, respectively; $\mu_a(E)$, $\mu_g(E)$ and $\mu_c(E)$ are the linear attenuation coefficients of adipose tissue, glandular tissue and microcalcification, respectively.

Because of the characteristics of diagnostic x-ray imaging physics shown in equation (1), only two unknowns can be solved for dual-energy digital mammography. During mammography, the breast is usually compressed to a uniform thickness T that can be easily measured. The contribution of microcalcifications to the total breast thickness can be ignored because the microcalcifications are small in size and sparsely present, i.e. $T \approx t_a + t_g$. With the total breast thickness T known, the three unknowns t_a, t_g and t_c can be expressed as two unknowns: glandular ratio $g = t_g/T \approx t_g/(t_a + t_g)$ and microcalcification thickness t_c (Kappadath and Shaw 2003). Now, equation (8) can be rewritten as

$$P(E) = P_0(E) \exp[-\mu_a(E) T - g(\mu_g(E) - \mu_a(E)) T - \mu_c(E) t_c] \tag{9}$$

In dual-energy imaging calculations, a reference signal I_r is needed in order to increase the dynamic range of the intensity values. The reference signal can be measured by a certain breast phantom. The exposure data f is defined as the logarithmic value of the ratio of transmitted exposure I to reference signal I_r. The high- and low-energy logarithmic intensities $f_h(t_c, g)$ and $f_l(t_c, g)$, respectively, are measured independently using x-ray beams at different kVps:

$$\begin{aligned} f_j(t_c, g) &= \ln(I_{rj}/I_j) \\ &= \ln(I_{rj}) - \ln\left(\int P_{0j}(E)\exp[-\mu_a(E)T - g(\mu_g(E) - \mu_a(E))T - \mu_c(E)t_c]Q(E)\,\mathrm{d}E\right), \\ & \qquad j = h, l. \end{aligned} \tag{10}$$

In this paper, we assume that there is no scatter because it can be well corrected (Kappadath and Shaw 2005). Therefore, g and t_c can be solved by a dual-energy imaging method.

2.3. Calibration phantom error formulae

In dual-energy digital mammography, phantoms for calibration are always different from real breast tissues that will be imaged. These differences lead to calibration phantom errors Δt_c of the microcalcification thickness and Δg of the glandular ratio.

When phantoms are used for calibration, equation (10) can be expressed as

$$\begin{aligned} f_j(t_c, g) &= \ln(I_{rj}/I_j) \\ &= \ln(I_{rj}) - \ln\left(\int P_{0j}(E)\exp\left[-\mu_a^{hu}(E)T - g\left(\mu_g^{hu}(E) - \mu_a^{hu}(E)\right)T - \mu_c^{hu}(E)t_c\right]Q(E)\,\mathrm{d}E\right) \\ &= \ln(I_{rj}) - \ln\left(\int P_{0j}(E)\exp\left[-\mu_a^{ph}(E)T - g'\left(\mu_g^{ph}(E) - \mu_a^{ph}(E)\right)T - \mu_c^{ph}(E)t_c'\right]Q(E)\,\mathrm{d}E\right), \\ & \qquad j = h, l \end{aligned} \tag{11}$$

where the second row of equation (11) represents the imaging of breast tissues and the third row represents the imaging of phantoms. The superscript '*hu*' indicates breast tissues while '*ph*' indicates phantoms. g and t_c represent the true glandular ratio and microcalcification thickness of the breast, respectively. Let g' and t_c' represent the calculated glandular ratio and microcalcification thickness of the phantoms:

$$g' = g + \Delta g, \tag{12}$$

$$t_c' = t_c + \Delta t_c, \tag{13}$$

where Δg and Δt_c are calibration phantom errors. The third row of equation (11) can be approximated by the first-order Taylor series expansion of variables g and t_c, so that Δg and Δt_c can be separated:

$$\begin{aligned} &\ln(I_{rj}) - \ln\left(\int P_{0j}(E)\exp\left[-\mu_a^{hu}(E)T - g\left(\mu_g^{hu}(E) - \mu_a^{hu}(E)\right)T - \mu_c^{hu}(E)t_c\right]Q(E)\,\mathrm{d}E\right) \\ &= \ln(I_{rj}) - \ln\left(\int P_{0j}(E)\exp\left[-\mu_a^{ph}(E)T - g\left(\mu_g^{ph}(E) - \mu_a^{ph}(E)\right)T - \mu_c^{ph}(E)t_c\right]Q(E)\,\mathrm{d}E\right) \\ &\quad + \beta_j^c \times \Delta t_c + \beta_j^g \times T \times \Delta g, \qquad j = h, l, \end{aligned} \tag{14}$$

where β_j^c and β_j^g are defined as

$$\beta_j^c = \frac{\int P_{0j}(E)\mu_c^{ph}(E)\exp\left[-\mu_a^{ph}(E)T - g\left(\mu_g^{ph}(E) - \mu_a^{ph}(E)\right)T - \mu_c^{ph}(E)t_c\right]Q(E)\,\mathrm{d}E}{\int P_{0j}(E)\exp\left[-\mu_a^{ph}(E)T - g\left(\mu_g^{ph}(E) - \mu_a^{ph}(E)\right)T - \mu_c^{ph}(E)t_c\right]Q(E)\,\mathrm{d}E}, \quad j = h, l \tag{15}$$

and

$$\beta_j^g = \frac{\int P_{0j}(E)\left(\mu_g^{ph}(E)-\mu_a^{ph}(E)\right)\exp\left[-\mu_a^{ph}(E)T-g\left(\mu_g^{ph}(E)-\mu_a^{ph}(E)\right)T-\mu_c^{ph}(E)t_c\right]Q(E)\,\mathrm{d}E}{\int P_{0j}(E)\exp\left[-\mu_a^{ph}(E)T-g\left(\mu_g^{ph}(E)-\mu_a^{ph}(E)\right)T-\mu_c^{ph}(E)t_c\right]Q(E)\,\mathrm{d}E},$$

$$j = h, l. \tag{16}$$

Let $\mu_c^{hu}(E) = \mu_c^{ph}(E) + \Delta\mu_c(E)$, $\mu_g^{hu}(E) = \mu_g^{ph}(E) + \Delta\mu_g(E)$, $\mu_a^{hu}(E) = \mu_a^{ph}(E) + \Delta\mu_a(E)$. By substituting the attenuation coefficients of phantoms for those of human breast on the left side of equation (14), expanding the left side, and eliminating the same terms on both sides, we have

$$\begin{aligned}
&\frac{\int P_{0j}(E)\Delta\mu_c(E)\exp\left[-\mu_a^{ph}(E)T - g\left(\mu_g^{ph}(E) - \mu_a^{ph}(E)\right)T - \mu_c^{ph}(E)t_c\right]Q(E)\,\mathrm{d}E}{\int P_{0j}(E)\exp\left[-\mu_a^{ph}(E)T - g\left(\mu_g^{ph}(E) - \mu_a^{ph}(E)\right)T - \mu_c^{ph}(E)t_c\right]Q(E)\,\mathrm{d}E} \times t_c \\
&\quad + \frac{\int P_{0j}(E)\Delta\mu_g(E)\exp\left[-\mu_a^{ph}(E)T - g\left(\mu_g^{ph}(E) - \mu_a^{ph}(E)\right)T - \mu_c^{ph}(E)t_c\right]Q(E)\,\mathrm{d}E}{\int P_{0j}(E)\exp\left[-\mu_a^{ph}(E)T - g\left(\mu_g^{ph}(E) - \mu_a^{ph}(E)\right)T - \mu_c^{ph}(E)t_c\right]Q(E)\,\mathrm{d}E} \\
&\qquad \times T \times g \\
&\quad + \frac{\int P_{0j}(E)\Delta\mu_a(E)\exp\left[-\mu_a^{ph}(E)T - g\left(\mu_g^{ph}(E) - \mu_a^{ph}(E)\right)T - \mu_c^{ph}(E)t_c\right]Q(E)\,\mathrm{d}E}{\int P_{0j}(E)\exp\left[-\mu_a^{ph}(E)T - g\left(\mu_g^{ph}(E) - \mu_a^{ph}(E)\right)T - \mu_c^{ph}(E)t_c\right]Q(E)\,\mathrm{d}E} \\
&\qquad \times T \times (1-g) \\
&= \beta_j^c \times \Delta t_c + \beta_j^g \times T \times \Delta g, \qquad j = h, l.
\end{aligned} \tag{17}$$

Define the symbols

$$\alpha_j^m = \frac{\int P_{0j}(E)\Delta\mu_m(E)\exp\left[-\mu_a^{ph}(E)T - g\left(\mu_g^{ph}(E) - \mu_a^{ph}(E)\right)T - \mu_c^{ph}(E)t_c\right]Q(E)\,\mathrm{d}E}{\int P_{0j}(E)\exp\left[-\mu_a^{ph}(E)T - g\left(\mu_g^{ph}(E) - \mu_a^{ph}(E)\right)T - \mu_c^{ph}(E)t_c\right]Q(E)\,\mathrm{d}E},$$

$$m = c, g, a; \qquad j = h, l, \tag{18}$$

and there is

$$\begin{aligned}
\beta_j^c \times \Delta t_c + \beta_j^g \times T \times \Delta g &= \alpha_j^c \times t_c + \alpha_j^g \times T \times g + \alpha_j^a \times T \times (1-g) \\
&= \alpha_j^c \times t_c + \left(\alpha_j^g - \alpha_j^a\right) \times T \times g + \alpha_j^a \times T, \qquad j = h, l,
\end{aligned} \tag{19}$$

where β_h^c and β_l^c are the average attenuation coefficients of microcalcification calibration phantom weighted by transmitted high- and low-spectra. β_h^g and β_l^g are the average attenuation coefficient differences between the glandular calibration phantom and the adipose calibration phantom weighted by transmitted high- and low-spectra. α_j^m ($m = c, g, a$; $j = h, l$) is the average attenuation coefficient difference between calibration phantoms and human breast for microcalcifications, glandular and adipose weighted by transmitted high- and low-spectra. In this paper, we focus on the calibration phantom errors caused by breast calibration phantoms and assume that α_h^c and α_l^c are zero. From equation (19), the calibration phantom errors Δt_c

Table 1. Elemental compositions (percentage per weight) of C and O for glandular and adipose tissues (Hammerstein *et al* 1979).

	Composition 1 (%)		Composition 2 (%)		Composition 3 (%)	
Element	Adipose	Glandular	Adipose	Glandular	Adipose	Glandular
C	68.1	30.5	51.3	10.8	61.9	18.4
O	18.9	55.6	35.7	75.3	25.1	67.7

and Δg can be determined as

$$\Delta t_c = \frac{\left[\left(\alpha_l^g - \alpha_l^a\right) g + \alpha_l^a\right] \times T \times \beta_h^g - \left[\left(\alpha_h^g - \alpha_h^a\right) g + \alpha_h^a\right] \times T \times \beta_l^g}{\beta_l^c \times \beta_h^g - \beta_h^c \times \beta_l^g}, \quad (20)$$

$$\Delta g = \frac{\left[\left(\alpha_h^g - \alpha_h^a\right) g + \alpha_h^a\right] \times \beta_l^c - \left[\left(\alpha_l^g - \alpha_l^a\right) g + \alpha_l^a\right] \times \beta_h^c}{\beta_l^c \times \beta_h^g - \beta_h^c \times \beta_l^g}. \quad (21)$$

3. Data for calculation

Using the formulae derived in section 2, the calibration phantom errors can be calculated using publicly available data. The imaging conditions are similar to those in Kappadath and Shaw (2003, 2005) and Lemacks *et al* (2002), which agree with the clinical mammography system. The x-ray spectra are 25 kVp and 50 kVp with a Mo anode and a 0.03 mm Mo filter. The spectra data are obtained from the classical handbook (Fewell and Shuping 1978). The detector consists of a CsI:Tl converter layer coupled with an aSi:H + TFT flat-panel detector. In our calculation, the scintillator thickness t_s is 45 mg cm^{-2} for CsI:Tl. All photons transmitted through the imaged object are assumed to be absorbed completely in the perfectly efficient converter layer (Lemacks *et al* 2002). The detector response function $Q(E)$ is defined as

$$Q(E) = A(E)E, \quad (22)$$

$$A(E) = 1 - \exp(-\mu_s(E)t_s), \quad (23)$$

where $\mu_s(E)$ is the mass attenuation coefficient of CsI (Berger *et al* 2005).

Hammerstein *et al* (1979) have determined the elemental compositions of glandular and adipose tissues for human breast. The composition per weight of H, N and P was well determined. However, the composition per weight of C and O presents a wide range of possible values. Table 1 lists two extreme compositions 1 and 2 and one general composition 3. In this paper, the composition per weight of C and O refers to 'composition 3' without specific notification. The densities equal to 0.93 g cm^{-3} for adipose tissue and 1.04 g cm^{-3} for glandular tissue.

Phantom materials are used for calibration. While polyethylene (CH_2) is commonly used for an adipose phantom material, PMMA ($C_5H_8O_2$) and acrylic ($C_3H_4O_2$) are often used for a glandular phantom material. Also, commercial breast tissue equivalent materials are available in the market. For example, breast adipose and glandular tissue equivalent materials from CIRS (Computerized Imaging Reference Systems, Inc., Norfolk, VA, USA) are based on Hammerstein *et al* (1979), and those from RMI (Radiation Measurements Inc., Madison, WI, USA) are based on White *et al* (1977). Our previous work (Mou and Chen 2007) showed that CIRS phantoms used in calibration lead to smaller calibration phantom errors compared with other phantoms. Therefore, we use CIRS phantoms in this paper. The elemental compositions and densities of CIRS phantoms and human breast are listed in table 2 (Byng *et al* 1998).

Table 2. Elemental compositions (percentage per weight) and densities of CIRS phantoms and breast tissues (Hammerstein *et al* 1979, Byng *et al* 1998).

Materials	Density (g cm^{-3})	Elemental compositions (%)							
		H	C	N	O	Cl	Ca	P	Al
CIRS adipose	0.924	11.8	76.0	1.2	9.8	1.2	–	–	–
Human adipose	0.93	11.2	61.9	1.7	25.1	–	–	0.1	–
CIRS glandular	1.04	10.9	70.2	1.2	12.5	1.1	0.6	–	3.5
Human glandular	1.04	10.2	18.4	3.2	67.7	–	–	0.5	–

Fandos-Morera *et al* (1988) analyzed the compositions of microcalcifications and setup possible relationships with malignant and benign lesions. Calcium oxalate (CaC_2O_4) is a common component of microcalcification in human breasts. In our study, calcium oxalate is employed as microcalcifications with a density of 2.20 g cm^{-3}. Based on the elemental compositions listed in table 2, mass attenuation coefficients of CIRS phantoms and breast tissues are calculated via the database of XCOM from NIST (Berger *et al* 2005). The breast thickness is assumed to be 5 cm.

4. Results

4.1. Calibration phantom error

Microcalcifications are relatively small in size, ranging from 1 mm to less than 100 μm, with most of them smaller than 500 μm. Therefore, we will focus on microcalcifications smaller than 500 μm with glandular ratio ranging from 0% to 100%.

CIRS phantoms are adopted for calibration. First, we calculate the average difference of linear attenuation coefficients between CIRS phantoms and breast tissues. According to the elemental compositions listed in table 2, we can obtain the mass attenuation coefficients using the XCOM database, and then calculate the average difference as

$$\text{Average Difference} = \frac{1}{40}\sum_{E=10\text{ kev}}^{50\text{ kev}} \frac{|(\mu(E)/\rho)^{ph}\rho^{ph} - (\mu(E)/\rho)^{hu}\rho^{hu}|}{(\mu(E)/\rho)^{hu}\rho^{hu}} \times 100\%, \tag{24}$$

where $\mu(E)/\rho$ is the mass attenuation coefficient and ρ is the mass density. In the energy range 10–50 keV, the average difference between CIRS phantoms and breast tissues is very small: 1.14% for adipose and 0.95% for glandular. Hence, the attenuation characteristics of CIRS phantoms can mimic those of breast tissues well.

Calibration phantom errors are calculated using equations (20) and (21) with the spectra data, detector response function, mass attenuation coefficients and densities of phantoms and breast tissues mentioned in section 3. Tables 3 and 4 list the calculated calibration phantom errors for different combinations of the microcalcification thickness and glandular ratio for composition 3, showing that the calibration phantom errors are large enough to seriously deteriorate the calculation precision.

4.2. Calibration phantom error when breast composition varying

The breast compositions of different individuals vary greatly. When calibration phantoms are fixed, the variations of different individuals result in different calibration phantom errors.

Table 3. Calibration phantom errors for the microcalcification thickness Δt_c (μm).

Glandular ratio	Microcalcification thickness t_c (μm)										
g (%)	0	50	100	150	200	250	300	350	400	450	500
0	−64	−64	−65	−66	−66	−67	−67	−67	−68	−69	−69
10	−11	−11	−12	−13	−14	−14	−15	−16	−16	−17	−18
20	45	40	40	39	38	37	36.	35	34	34	33
30	93	92	91	90	89	88	87	86	85	84	83
40	144	142	141	140	139	138	137	136	135	134	133
50	193	192	191	190	188	187	186	185	184	183	182
60	243	241	240	239	237	236	235	233	232	231	230
70	291	290	288	287	286	284	283	281	280	278	277
80	339	338	336	335	333	332	330	328	327	326	324
90	387	385	383	382	380	378	377	375	374	372	370
100	433	432	430	428	426	425	423	421	419	418	416

Table 4. Calibration phantom errors for glandular ratio Δg (%).

Glandular	Microcalcification thickness t_c (μm)										
ratio g (%)	0	50	100	150	200	250	300	350	400	450	500
0	1.2	1.3	1.3	1.4	1.4	1.4	1.5	1.5	1.6	1.6	1.6
10	−2.4	−2.3	−2.2	−2.20	−2.1	−2.1	−2.0	−2.0	−2.0	−1.9	−1.8
20	−5.9	−5.8	−5.8	−5.7	−5.6	−5.6	−5.5	−5.5	−5.4	−5.4	−5.3
30	−9.4	−9.3	−9.2	−9.2	−9.1	−9.0	−9.0	−8.9	−8.8	−8.8	−8.7
40	−12.8	−12.8	−12.7	−12.6	−12.5	−12.4	−12.4	−12.3	−12.2	−12.2	−12.1
50	−16.2	−16.1	−16.0	−16.0	−16.0	−15.8	−15.7	−15.6	−15.6	−15.5	−15.4
60	−19.6	−19.5	−19.4	−19.3	−19.2	−19.1	−19.0	−18.9	−18.8	−18.7	−18.7
70	−22.9	−22.8	−22.7	−22.6	−22.5	−22.4	−22.3	−22.2	−22.1	−22.0	−22.2
80	−26.1	−26.0	−25.9	−25.8	−25.7	−25.6	−25.5	−25.4	−25.3	−25.2	−25.1
90	−29.3	−29.2	−29.1	−29.0	−28.9	−28.8	−28.6	−28.5	−28.4	−28.3	−28.2
100	−32.5	−32.4	−32.2	−32.1	−32.0	−31.9	−31.8	−31.6	−31.5	−31.4	−31.3

Tables 5 and 6 list the calibration phantom errors Δt_c and Δg for the three compositions listed in table 1 when the microcalcification thickness is 250 μm and the glandular ratio ranges from 0% to 100%. In tables 5 and 6, calibration phantom errors have significant differences for different compositions. For example, when the glandular ratio is 50%, the error Δt_c varies from −270 μm to 628 μm as the breast composition changes from composition 1 to composition 2. Therefore, the true microcalcification thickness cannot be determined if the breast composition is unknown. In other words, the computed pair (t_c', g') will map to different combinations (t_c, g) of the microcalcification thickness and glandular ratio for different breast compositions. Figure 1 illustrates how the computed pair (t_c', g') maps to a true pair (t_c, g) when breast composition varies. Two cases are demonstrated, which are (850 μm, 35%) and (750 μm, 60%) of the computed pair (t_c', g'). As demonstrated in figure 1, for the computed pair (t_c', g'), the corresponding true value (t_c, g) changes along a line segment connecting the two extreme cases of compositions 1 and 2. Obviously, it is impossible for the mapped real pair (−130 μm, 114%) of composition 2 to have the case (750 μm, 60%). In practice, the computed pair cannot be (750 μm, 60%) when the breast tissue is of composition 2. Here, we just plot it in the figure for clarity. In practice, the breast composition will change between the two extreme compositions 1 and 2 in the shadow.

Table 5. Calibration phantom errors for the microcalcification thickness Δt_c (μm).

Breast composition	Glandular ratio g (%)										
	0	10	20	30	40	50	60	70	80	90	100
Composition 1	−360	−341	−322	−304	−287	−270	−254	−238	−222	−207	−193
Composition 2	429	470	511	551	590	628	666	704	741	777	813
Composition 3	−67	−14	37	88	138	187	236	284	332	378	425

Table 6. Calibration phantom errors for glandular ratio Δg (%).

Breast composition	Glandular ratio g (%)										
	0	10	20	30	40	50	60	70	80	90	100
Composition 1	14.8	12.7	10.6	8.6	6.6	4.7	2.8	0.9	−0.9	−2.8	−4.5
Composition 2	−20.9	−23.9	−26.8	−29.7	−32.6	−35.4	−38.2	−41.0	−43.7	−46.4	−49.0
Composition 3	1.4	−2.1	−5.6	−9.0	−12.4	−15.8	−19.1	−22.4	−25.6	−28.8	−31.9

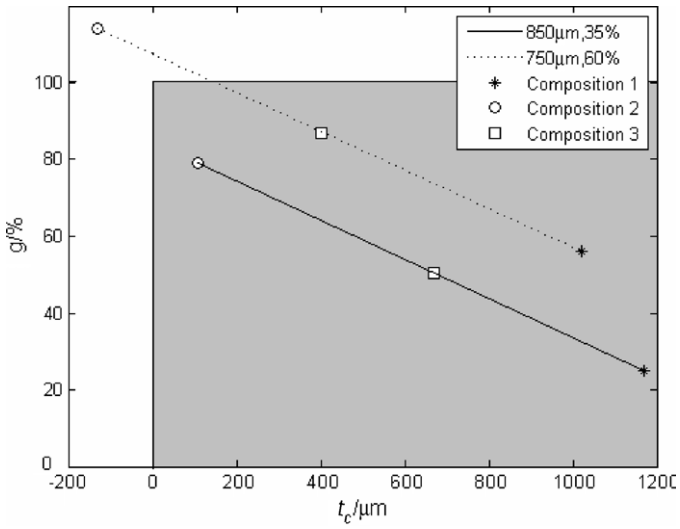

Figure 1. Maps of computed pair (t_c', g') to real pair (t_c, g) when breast composition changes.

5. Discussion

5.1. Magnitude of the calibration phantom error

The data calculation results in section 4 show that the calibration phantom errors are large enough that they greatly decrease the calculation precision of dual-energy digital mammography. Although the used CIRS phantoms have only about a 1% difference in linear attenuation coefficients compared to the general breast tissue composition, the calibration phantom errors could reach tens to hundreds of percents. For example, when a microcalcification is 250 μm, the calibration phantom error Δt_c ranges from −27% (−67 μm) to 170% (425 μm) as the glandular ratio increases from 0% to 100%. Calibration

phantom errors also change significantly as the composition varies. For an imaged object of 250 μm microcalcification and 50% glandular ratio, the calibration phantom error Δt_c is -270 μm for composition 1 and 628 μm for composition 2.

Because our imaging conditions are similar to those of existing references (Kappadath and Shaw 2003, 2005, Lemacks *et al* 2002), we can compare our results to the reported results in these papers. Lemacks *et al* (2002) investigated the errors caused by quantum noise of the detector with normal exposure dose. They showed that a 250 μm microcalcification could be subject to random noise of 80 μm for a 5 cm breast with 50% glandular ratio. However, our study shows that the corresponding calibration phantom error of the microcalcification thickness is 187 μm for composition 3 and even bigger for compositions 1 (-270 μm) and 2 (628 μm). Thus, the calibration phantom errors are much greater than errors caused by detector quantum noise. Kappadath and Shaw (2003) concluded that the mean fitting error is $\sim$50 μm and the max fitting error is $\sim$150 μm for the microcalcification thickness when adopting a cubic or conic function. In our study, when the breast is of composition 3, the mean calibration phantom error for the microcalcification thickness is 192 μm and the maximum is 433 μm (see table 3). When the breast is of composition 2, the maximum calibration phantom error will reach 813 μm (see table 5). Obviously, calibration phantom errors are much greater than the fitting errors in dual-energy digital mammography. Kappadath and Shaw (2005) showed that microcalcifications of 300–355 μm can be clearly seen while microcalcifications of 250–280 μm are barely visible in dual-energy calcification images after scatter and nonuniformity corrections. Due to the existence of large calibration phantom errors and the diversity of breast compositions, the microcalcification thickness threshold cannot be determined even if both scatter and nonuniformity corrections are well addressed. In summary, a calibration phantom error is dominant among all kinds of errors in dual-energy digital mammography calculation.

5.2. Property of the calibration phantom error

From tables 3 and 4, we can see that for a fixed glandular ratio, calibration phantom errors are almost unchanged when the microcalcification thickness changes from 0 μm to 500 μm. For example, Δt_c changes from 193 μm to 182 μm and Δg changes from -16.2% to -15.4% when the microcalcification thickness ranges from 0 μm to 500 μm with the glandular ratio being 50%. The variation ratios are 5.7% for Δt_c and 4.9% for Δg. In fact, Δt_c and Δg are calculated from equations (20) and (21) which are formed by $\alpha_j^m (m = c, g, a;\ j = h, l)$, $\beta_j^m (m = c, g;\ j = h, l)$, g and T, where α_j^m and β_j^m are the attenuation coefficients and the corresponding differences weighted by the transmitted high- and low-spectra. The transmitted high- and low-spectra are slightly affected by the microcalcification thickness because of their small size, and hence α_j^m and β_j^m change little when the microcalcification thickness changes. Therefore, for a fixed glandular ratio g, the calibration phantom errors Δt_c and Δg are almost unchanged when the microcalcification thickness changes from 0 μm to 500 μm.

5.3. Analysis of physical meaning for the calibration phantom error

In section 2.1, we showed that the attenuation of an imaged object can be described by equation (4), and the pair (b_d, b_p) can be used to represent the attenuation of the object. In mammography, the imaged object is breast tissues plus microcalcifications. We have

$$b_d = b_{d\_\text{breast}} + b_{d\_mc}, \qquad b_p = b_{p\_\text{breast}} + b_{p\_mc} \tag{25}$$

where $(b_{d\_\text{breast}}, b_{p\_\text{breast}})$ and (b_{d_mc}, b_{p_mc}) represent the attenuation of the breast tissues and microcalcifications, respectively. As shown in figure 2, we use the vectors $\boldsymbol{OA}$, $\boldsymbol{OB}$ and $\boldsymbol{BA}$ to represent (b_d, b_p), $(b_{d\_\text{breast}}, b_{p\_\text{breast}})$ and (b_{d_mc}, b_{p_mc}) respectively.

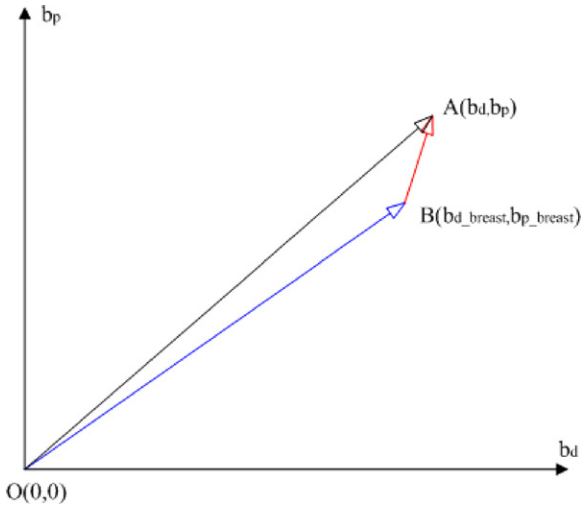

Figure 2. Sketch of the attenuation characteristics in mammography.

We define a quantity of attenuation gradient (*AG*) as follows:

$$AG = b_p/b_d. \tag{26}$$

In our study, the component of microcalcification is calcium oxalate (CaC_2O_4). The *AG* for microcalcification can be written as

$$\begin{aligned} AG_{mc} = b_{p\_mc}/b_{d\_mc} &= (b_{pu\_CaC_2O_4} \times t_c)/(b_{du\_CaC_2O_4} \times t_c) \\ &= b_{pu\_CaC_2O_4}/b_{du\_CaC_2O_4}. \end{aligned} \tag{27}$$

According to equation (1), $b_{du\_CaC_2O_4}$ and $b_{pu\_CaC_2O_4}$ only relate to the linear attenuation coefficient of calcium oxalate. Therefore, AG_{mc} is a fixed value in our study.

Now, we adopt a 250 μm microcalcification with 50% glandular ratio of composition 3 as the imaged object. Recall that table 3 shows that the calibration phantom error Δt_c is 187 μm. Figure 3 analyzes Δt_c. Because the breast thickness T is known and fixed and there exist attenuation differences between the breast tissues and the calibration phantoms, the pair (b_d, b_p) of the breast tissues and calibration phantoms will change along two independent line segments. The pair (b_d, b_p) of the breast tissues changes along the blue dotted line segment CD when glandular ratio varies from 0% to 100%. The point C corresponds to 0% glandular ratio, while point D corresponds to 100% glandular ratio. Correspondingly, the pair (b_d, b_p) of CIRS phantoms changes along the mauve dotted line segment C_cD_c. However, the real pair (b_d, b_p) of this imaged object is point A. From point A, we can draw a line with gradient AG_{mc} to represent the attenuation of microcalcification. This line crosses CD and C_cD_c, generating two intersection points B and B_c. Note that point B maps to the attenuation of breast tissues of glandular ratio 50%, and the vector $\boldsymbol{BA}$ represents the attenuation of real microcalcification. Because point B_c maps to the attenuation of CIRS phantoms with calculated glandular ratio g' (34.2%), the vector $\boldsymbol{B_CA}$ represents the attenuation of the calculated microcalcification with thickness t_c' (437 μm). The vector $\boldsymbol{B_CB}$ represents the calibration phantom error Δt_c (187 μm), which is caused by the differences between breast tissues and calibration phantom. Because the size of the microcalcification is relatively small, the attenuation of the microcalcification is much smaller compared with that of breast tissues or phantoms, and the point A is always

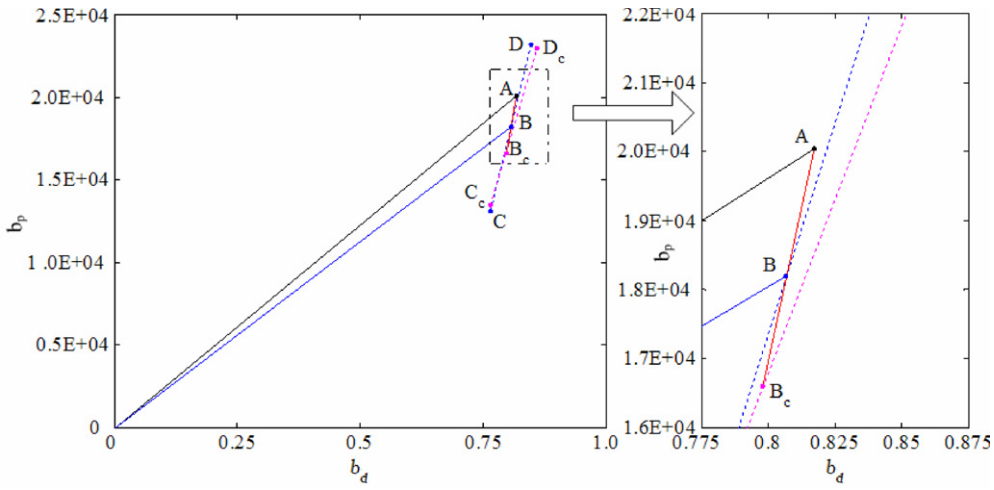

Figure 3. Physical meaning of calibration phantom errors.

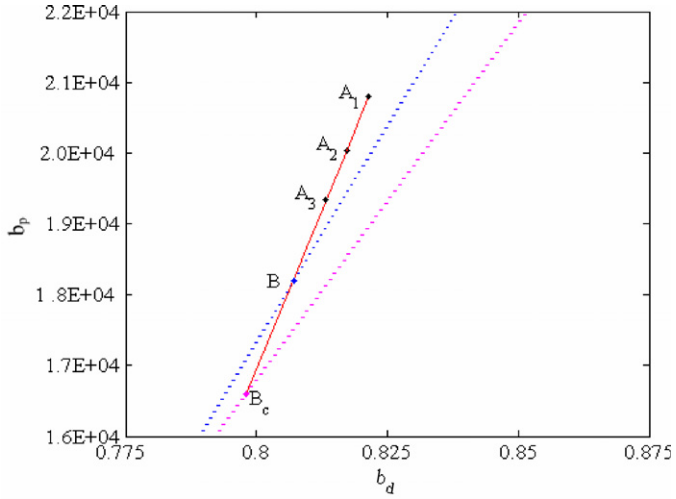

Figure 4. Calibration phantom errors of different microcalcification thicknesses.

close to the blue dotted line segment. Therefore, the length of $\boldsymbol{B_CB}$ is relatively long compared with that of $\boldsymbol{BA}$, which implies big values of the calibration phantom error Δt_c.

As can be seen in tables 3 and 4, the calibration phantom errors are almost unchanged when the glandular ratio is fixed and the microcalcification thickness varies. This phenomenon can be explained by figure 4. The blue and mauve dotted line segments, point B and point B_c, have the same meaning as in figure 3. For a glandular ratio of 50%, point B is fixed on the blue dotted line segment which maps to the attenuation of breast tissues. We can draw a red line that crosses point B with gradient AG_{mc}. The vector $\boldsymbol{B_CB}$ represents the calibration phantom error Δt_c when the true glandular ratio is 50%. The three points A_1, A_2 and A_3 correspond to attenuations of three imaged objects with 50% glandular ratio and microcalcification of 150 μm, 250 μm and 350 μm, respectively. All of them are located on the red line that crosses

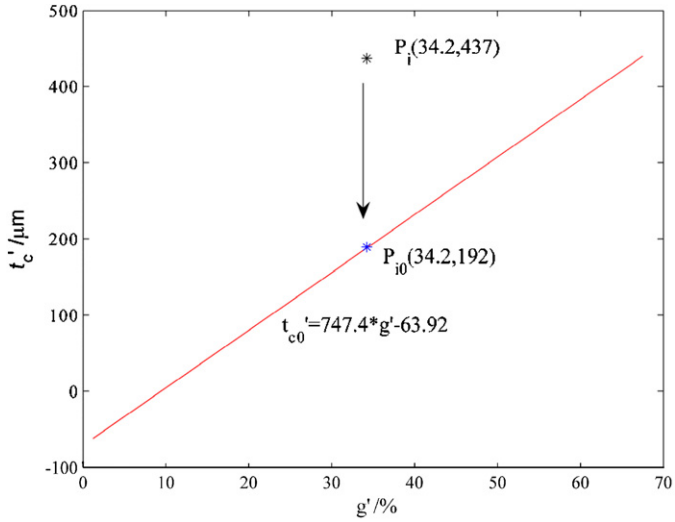

Figure 5. Demonstration of the correction method for calibration phantom error Δt_c.

B and B_c, which implies the same calibration phantom errors. Therefore, there will be the same calibration phantom errors if the imaged objects have the same glandular ratio.

However, there still exist small differences among the calibration phantom errors that can be seen in tables 3 and 4 when the glandular ratio is constant. These differences come from the dependence of energy during the calculation of b_p and b_d. From equations (3)–(5), we can see that b_p and b_d are almost independent of energy. If b_p and b_d were independent of energy completely, there would be no difference in the calibration phantom errors. Actually, b_p and b_d are weakly dependent on energy (Gingold and Hasegawa 1992), and both b_p and b_d are influenced by the transmitted spectra. When the microcalcification thickness changes, the transmitted high- and low-energy spectra will also change slightly. Consequently, b_p and b_d will change a little; hence, there are small differences in calibration phantom errors.

5.4. Error correction method

Omitting the small difference caused by energy dependence, the calibration phantom errors will be constant if the imaged objects have the same glandular ratio. This property suggests a correction method for the calibration phantom error Δt_c.

In dual-energy digital mammography, for an imaged breast, we can calculate (g', t_c') of each pixel pair based on the high- and low-energy image and set up a coordinate system with the horizontal axis as g' and vertical axis as t_c'. (g', t_c') of each pixel pair can be positioned in the coordinate system. Obviously, the computed t_c' of the non-microcalcification pixel pair equals their Δt_c.

In full-field digital mammography, there are several millions of pixels in an image. Because microcalcifications are small and sparsely present in breast tissues, most pixels in mammogram are non-microcalcification pixels. With millions of pairs in the coordinate system, a curve can be fitted. (g', t_c') on the fitted curve can be considered as those correspond to non-microcalcification pixel pairs. Therefore, t_c' of (g', t_c') on the fitted curve is the calibration phantom error Δt_c.

Recall that the calibration phantom errors Δt_c and Δg are constant if the imaged objects have the same glandular ratio. Denoted by (g_i', t_{ci}') the calculated results for any pixel pair P_i in dual-energy mammograms, we can find the corresponding pair (g_i', t_{ci0}') on the fitted curve. Therefore, $t_{ci\,0}'$ is the calibration phantom error Δt_{ci} of the pixel pair P_i. The true microcalcification thickness of the pixel pair P_i corresponds to $t_{ci} = t_{ci}' - t_{ci\,0}'$. For example, the fitted red curve $t_{c0}' = 747.4{*}g' - 63.92$ in figure 5 corresponds to the data in tables 3 and 4. For pixel pair P_i, the true microcalcification thickness and glandular ratio are 250 μm and 50%, respectively. The calculated pair (g_i', t_{ci}') of P_i is (34.2%, 437 μm), as shown in figure 5. Substituting g_i' (34.2%) into the expression of the fitted curve, $t_{ci\,0}'$ (192 μm) can be obtained. The corresponding pair P_{i0} (g_i', t_{ci0}') is shown as the blue asterisk in figure 5. $t_{ci\,0}'$ equals the Δt_{ci} of P_i. After the calibration phantom error is corrected, the computed microcalcification thickness is 245 μm, which is very close to the true thickness of 250 μm. Using this method, we can correct the calibration phantom error Δt_c for all pixel pairs.

6. Conclusion

Dual-energy digital mammography can be used to suppress the contrast between adipose and glandular tissues to improve the detection of microcalcifications. It is a prospective technique to reduce the high false-negative rate of microcalcification detection in normal mammography. In this paper, the formulae of calibration phantom errors, which are caused by the differences of linear attenuation coefficients between calibration phantoms and breast tissues, were derived based on the imaging physical model. Based on the publicly available composition data of breast tissues and phantom materials, we calculated the calibration phantom errors and compared them with other types of errors in dual-energy digital mammography. Our results show that the attenuation differences between breast tissues and calibration phantoms can lead to significantly large calibration phantom errors in the order of tens to hundreds of percent, even if CIRS phantoms are adopted. A calibration phantom error is the major source of error in dual-energy digital mammography and varies for different breast compositions of different individuals.

After deeply investigating the physical meaning of calibration phantom errors, we found that calibration phantom errors are constant for a fixed glandular ratio. With this property and using all the pixels in the images, we suggested a correction method for the calibration phantom error of the microcalcification thickness. The results show that the large calibration phantom error of the microcalcification thickness can be corrected.

Acknowledgments

The project is partially supported by the National Science Fund of China (no 60472004 and no 60551003), the fund of the Ministry of Education of China (no 106143 and no NCET-05-0828), the fund of USA National Institutes of Health (EB007288) and the fund of ICRG of Hong Kong Polytechnic University (YG-79). The authors thank Ms Lena Ye for editorial refinements.

References

Alvarez R E and Macovski A 1976 Energy-selective reconstruction in x-ray computerized tomography *Phys. Med. Biol.* **21** 733–44

Berger M J, Hubbell J H, Seltzer S M, Chang J, Coursey J S, Sukumar R and Zucker D S 2005 XCOM: Photon Cross Section Database (version 1.3) available at: http://physics.nist.gov/xcom (Gaithersburg, MD: National Institute of Standards and Technology)

Bliznakova K, Kolitsi Z and Pallikarakis N 2006 Dual-energy mammography: simulation studies *Phys. Med. Biol.* **51** 4497–515

Boone J M, Shaber G S and Tecotzky M 1990 Dual-energy mammography: a detector analysis *Med. Phys.* **17** 665–75

Brandan M E and Ramirez-R V 2006 Evaluation of dual-energy subtraction of digital mammography images under conditions found in a commercial unit *Phys. Med. Biol.* **51** 2307–20

Brettle D S and Cowen A R 1994 Dual-energy digital mammography using stimulated phosphor computed radiography *Phys. Med. Biol.* **39** 1989–2004

Brody W R, Butt G, Hall A and Macovski A 1981 A method for selective tissue and bone visualization using dual energy scanned projection radiography *Med. Phys.* **8** 353–7

Byng J W, Mainprize J G and Yaffe M J 1998 X-ray characterization of breast phantom materials *Phys. Med. Biol.* **43** 1367–77

Cardinal H N and Fenster A 1990 An accurate method for direct dual-energy calibration and decomposition *Med. Phys.* **17** 327–41

Chakraborty D P and Barnes G T 1989 An energy sensitive cassette for dual-energy mammography *Med. Phys.* **16** 7–13

Fandos-Morera A, Prats-Esteve M, Tura-Soteras J M and Traveria-Cros A 1988 Breast tumors: composition of microcalcifications *Radiology* **169** 325–7

Fewell T R and Shuping R E 1978 *Handbook of Mammographic X-ray Spectra* (Rockville, MD: Bureau of Radiological Health) pp 25–70

Gingold E L and Hasegawa B H 1992 Systematic bias in basis material decomposition applied to quantitative dual-energy x-ray imaging *Med. Phys.* **19** 25–33

Hammerstein G R, Miller D W, White D R, Masterson M E, Woodward H Q and Laughlin J S 1979 Absorbed radiation dose in mammography *Radiology* **130** 485–91

Johns P C, Drost D J, Yaffe M J and Fenster A 1985 Dual-energy mammography: initial experimental results *Med. Phys.* **12** 297–304

Johns P C and Yaffe M J 1985 Theoretical optimization of dual-energy x-ray imaging with application to mammography *Med. Phys.* **12** 289–96

Kappadath S C and Shaw C C 2003 Dual-energy digital mammography: calibration and inverse-mapping techniques to estimate calcification thickness and glandular-tissue ratio *Med. Phys.* **30** 1110–7

Kappadath S C and Shaw C C 2004 Quantitative evaluation of dual-energy digital mammography for calcification imaging *Phys. Med. Biol.* **49** 2563–76

Kappadath S C and Shaw C C 2005 Dual-energy digital mammography for calcification imaging: scatter and nonuniformity corrections *Med. Phys.* **32** 3395–408

Kappadath S C, Shaw C, Lai C J, Liu X and Whitman G 2004 Dual-energy digital mammography for calcification imaging: theory and implementation *Proc. SPIE* **5368** 751–60

Kappadath S C, Shaw C C, Lai C J, Liu X, Whitman G J and Yang W T 2005 Dual-energy digital mammography for calcification imaging: improvement by post-image processing *Proc. SPIE* **5745** 1342–50

Lehmann L A, Alvarez R E, Macovski A and Brody W R 1981 Generalized image combinations in dual KVP digital radiography *Med. Phys.* **8** 659–67

Lemacks M R, Kappadath S C, Shaw C C, Liu X and Whitman G J 2002 A dual-energy technique for microcalcification imaging in digital mammography: a signal-to-noise analysis *Med. Phys.* **29** 1739–51

Mou X Q and Chen X 2007 Error analysis of calibration materials on dual-energy mammography *Proc. 10th Int. Conf. on Medical Image Computing and Computer Assisted (Brisbane, Australia) LNCS* **Vol 4792** pp 596–603

Soo M S, Rosen E L, Xia J Q, Ghate S and Baker J A 2005 Computer-aided detection of amorphous calcifications *Am. J. Roentgenol.* **184** 887–92

Taibi A, Fabbri S, Baldelli P, di Maggio C, Gennaro G, Marziani M, Tuffanelli A and Gambaccini M 2003 Dual-energy imaging in full-field digital mammography: a phantom study *Phys. Med. Biol.* **48** 1945–56

White D R, Martin R J and Darlinson R 1977 Epoxy resin based tissue substitutes *Br. J. Radiol.* **50** 814–21